












## RESEARCH ARTICLE

# Engineering the catalytic activity of an Antarctic PET-degrading enzyme by loop exchange

Paula Blázquez-Sánchez<sup>1,2,3</sup>  | Jhon A. Vargas<sup>4</sup>  | Adriano A. Furtado<sup>4</sup>  | Aransa Griñen<sup>1,2</sup> | Diego A. Leonardo<sup>4</sup>  | Susana A. Sculaccio<sup>4</sup>  | Humberto D'Muniz Pereira<sup>4</sup>  | Christian Sonnendecker<sup>3</sup>  | Wolfgang Zimmermann<sup>3</sup>  | Beatriz Diez<sup>5,6,7</sup>  | Richard C. Garratt<sup>4</sup>  | César A. Ramírez-Sarmiento<sup>1,2</sup> 

<sup>1</sup>Institute for Biological and Medical Engineering, Schools of Engineering, Medicine and Biological Sciences, Pontificia Universidad Católica de Chile, Santiago, Chile

<sup>2</sup>ANID—Millennium Science Initiative Program, Millennium Institute for Integrative Biology (iBio), Santiago, Chile

<sup>3</sup>Institute of Analytical Chemistry, Leipzig University, Leipzig, Germany

<sup>4</sup>São Carlos Institute of Physics, University of São Paulo, São Carlos, Brazil

<sup>5</sup>Department of Molecular Genetics and Microbiology, School of Biological Sciences, Pontificia Universidad Católica de Chile, Santiago, Chile

<sup>6</sup>Center for Climate and Resilience Research (CR)<sup>2</sup>, Santiago, Chile

<sup>7</sup>Millennium Institute Center for Genome Regulation (CGR), Santiago, Chile

## Correspondence

César A. Ramírez-Sarmiento, Institute for Biological and Medical Engineering, Schools of Engineering, Medicine and Biological Sciences, Pontificia Universidad Católica de Chile, Av. Vicuña Mackenna 4860, 7820436, Santiago, Chile.  
Email: [cesar.ramirez@uc.cl](mailto:cesar.ramirez@uc.cl)

Richard C. Garratt, São Carlos Institute of Physics, University of São Paulo, Av. Trabalhador São-Carlense 400, São Carlos, São Paulo 13566-590, Brazil.  
Email: [richard@ifsc.usp.br](mailto:richard@ifsc.usp.br)

## Funding information

National Agency for Research and Development (ANID) and São Paulo Research Foundation (FAPESP) PCI ANID-FAPESP, Grant/Award Number: 2019/13259-9; ANID Millennium Science Initiative Program, Grant/Award Numbers: ICN17\_022, ICN2021\_044; Instituto Antártico Chileno (INACH), Grant/Award Numbers: DG\_11\_18, RT\_04\_19; ANID doctoral scholarships, Grant/Award Numbers: 21220450, 21191979; CAPES Masters' scholarship, Grant/Award Number:

## Abstract

Several hydrolases have been described to degrade polyethylene terephthalate (PET) at moderate temperatures ranging from 25°C to 40°C. These mesophilic PET hydrolases (PETases) are less efficient in degrading this plastic polymer than their thermophilic homologs and have, therefore, been the subject of many protein engineering campaigns. However, enhancing their enzymatic activity through rational design or directed evolution poses a formidable challenge due to the need for exploring a large number of mutations. Additionally, evaluating the improvements in both activity and stability requires screening numerous variants, either individually or using high-throughput screening methods. Here, we utilize instead the design of chimeras as a protein engineering strategy to increase the activity and stability of Mors1, an Antarctic PETase active at 25°C. First, we obtained the crystal structure of Mors1 at 1.6 Å resolution, which we used as a scaffold for structure- and sequence-based chimeric design. Then, we designed a Mors1 chimera via loop exchange of a highly divergent active site loop from the thermophilic leaf-branch compost cutinase (LCC) into the equivalent region in Mors1. After restitution of an active site disulfide bond into this chimera, the enzyme exhibited a shift in optimal temperature for activity to 45°C and an increase in fivefold in PET hydrolysis when compared with wild-type Mors1 at 25°C. Our results serve as a proof of concept

Reviewing Editor: Jeanine Amacher

88887.635854/2021-00; Supercomputing infrastructure of the NLHPC, Grant/Award Number: ECM-02

of the utility of chimeric design to further improve the activity and stability of PETases active at moderate temperatures.

#### KEYWORDS

mesophilic enzymes, PET hydrolases, plastics, polyethylene terephthalate, protein engineering

## 1 | INTRODUCTION

Plastic waste, primarily from packaging and textiles, constitutes an environmental problem due to its severe accumulation in landfills and oceans (Geyer et al., 2017). Their primary sources are single-use or short-lifetime consumer plastics such as polyethylene terephthalate (PET), which accounts for 20% of the plastics used for packaging and 70% of fiber production worldwide (Geyer et al., 2017). Consistently, PET is one of the predominant polymers in post-consumer domestic plastic waste, above polyethylene and polypropylene (Schyns & Shaver, 2021).

In this context, the discovery of enzymes that degrade PET into its constituent monomers, ethylene glycol (EG) and terephthalic acid (TPA), known as PET hydrolases (PETases), has emerged as a promising biological approach for plastic recycling (Wei & Zimmermann, 2017). Most known PETases are thermophilic, with optimal activities near the glass transition temperature of PET (~65°C) (Wei & Zimmermann, 2017) where the polymer chains become more flexible and are prone to enzymatic hydrolysis (Mueller, 2006). Nevertheless, in recent years several enzymes have been described to degrade PET at moderate temperatures: 25°C, in the case of Mors1 from the Antarctic-inhabiting bacteria *Moraxella* sp. TA144 (Mors1) (Blázquez-Sánchez et al., 2022); 30°C, in the case of Ple628 and Ple629 from a marine microbial consortium (Li et al., 2022; Meyer Cifuentes et al., 2022) and PE-H from *Pseudomonas aestusnigri* (Bollinger et al., 2020); and 40°C for the PETase from *Ideonella sakaiensis* 201-F6 (*IsPETase*) (Yoshida et al., 2016).

Protein engineering has successfully improved the activity of enzymes that work at moderate temperatures, with *IsPETase* being used as a chassis for most strategies. For example, the thermal stability of *IsPETase* was improved through rational design, leading to a triple mutant (*IsPETase*<sup>TS</sup>) with 14-fold increased activity and 9°C higher melting temperature ( $T_m$ ) compared with the wild-type (WT) enzyme (Son et al., 2019). A greedy protein engineering strategy (GRAPE), based on computational design to identify single-point substitutions that would improve thermal stability, led to a variant termed DuraPETase, containing 10 substitutions and showing an

increased degradation efficiency and 31°C higher  $T_m$  compared with *IsPETase* (Cui et al., 2021).

Successes in *IsPETase* engineering have been also propelled by directed evolution (Bell et al., 2022) and machine learning (Lu et al., 2022). Directed evolution involved screening over 13,000 enzyme variants from *IsPETase*<sup>TS</sup> producing HotPETase, with 36°C higher  $T_m$  and about 43-fold higher activity than *IsPETase*<sup>TS</sup> at 65°C, whereas a machine learning-based algorithm (Shroff et al., 2020) identified three substitutions on *IsPETase*<sup>TS</sup> that led to the design of FAST-PETase, a variant with 38-fold higher activity at 50°C (Lu et al., 2022).

While successful, most of these methods require an intensive screening effort to identify an enzyme variant that outperforms the WT enzyme. For example, only one of the seven mutants tested for PE-H showed increased PET hydrolysis (Bollinger et al., 2020), and the implementation of the GRAPE strategy required the experimental characterization of 85 single-point variants before designing an enzyme with multiple substitutions, whereas directed evolution requires the implementation of a high-throughput screening strategy to analyze the degradation products for thousands of variants (Bell et al., 2022). In contrast, chimeric design (Romero & Arnold, 2009), which recombines equivalent parts of homologous proteins based on structural information introducing multiple mutations at once, is less disruptive and generates functional proteins with much higher frequency than random mutations (Drummond et al., 2005; Romero & Arnold, 2009).

In this work, we test this chimeric design approach on Mors1, a PETase active at 25°C for which we solved its crystal structure at 1.6 Å resolution. As a proof of concept, we targeted the highly divergent extended loop in the catalytic site of these PETases (Joo et al., 2018) through loop exchange (Nestl & Hauer, 2014). We substituted the loop connecting  $\beta 8$ - $\alpha 6$  with a shorter one from a highly efficient PET-degrading cutinase, LCC, which has an optimum temperature of activity of ~70°C (Chen et al., 2021), to generate a chimera. Our results show that this loop exchange, followed by restitution of an active site disulfide bond lost in the process, resulted in an increase of the optimal activity temperature from 25°C to 45°C, accompanied by a remarkable fivefold

enhancement in catalytic activity against amorphous PET films at 45°C compared with the activity at 25°C. Lastly, molecular dynamic (MD) simulations of the WT enzyme and the loop exchanged variant suggest that the increase in activity is due to changes in local flexibility in the extended loop and in neighboring active site regions.

## 2 | RESULTS

### 2.1 | Unique structure and sequence features of Mors1 compared with other PETases

To enable the protein engineering of Mors1 using loop exchange, we first solved the three-dimensional structure of the WT enzyme by X-ray crystallography. After optimization of the soluble expression of Mors1 (see Materials and Methods) and 8 months of sitting-drop vapor diffusion crystallization at 20°C in a solution containing 0.8 mg/mL of protein and 1.4 M sodium malonate dibasic monohydrate at pH 7.0, with a final volume of 0.6  $\mu$ L, crystals were successfully obtained for diffraction. The crystals belong to space group  $P2_13$  and the structure was solved by molecular replacement to a resolution of 1.6 Å, using an AlphaFold2-predicted structure of Mors1 as a search model, and refined to final  $R_{work}$  and  $R_{free}$  values of 0.16 and 0.18, respectively. All data collection and quality control parameters are within the expected values (Table 1).

There are two polypeptide chains in the asymmetric unit of the crystal, which are found interacting through active site residues. We employed PDBePISA (Krissinel & Henrick, 2007) to determine if these interactions were likely to be stable. This analysis shows that the free energy for dissociation of the assembly is  $-1.2$  kcal/mol, suggesting that the biological assembly of Mors1 is likely a monomer in solution (Figure 1). This was also confirmed by size exclusion chromatography coupled with multi-angle light scattering (SEC-MALS) (Figure S1).

In general, the crystal structure of Mors1 was almost identical to its PET-degrading enzyme homologs, with a canonical  $\alpha/\beta$ -hydrolase fold comprising a central  $\beta$ -sheet of 9 strands surrounded by 6  $\alpha$ -helices (Figure 1a,b). The Ser-His-Asp catalytic triad is conserved, and binding subsite 2 is mostly compatible with type IIa PETases (Joo et al., 2018). However, there is a substitution of a serine (S268) instead of an asparagine which is generally conserved in all type II PETase-like enzymes, to which Mors1 belongs. Furthermore, the mainchain of subsite 2 together with the asparagine rotamer is also largely conserved, indicating low conformational variation in the region as a whole (Figure 1b,c). S268, therefore, stands out as an apparently unique feature of Mors1. In subsite I, on the

TABLE 1 X-ray data collection and structure refinement statistics.

Mors1	
X-ray source	Sirius MANACA
Detector	Pilatus 2 M
Cell parameters: a, b, and c (Å)	131.18, 131.18, and 131.18
Cell parameters: $\alpha$ , $\beta$ , and $\gamma$ (°)	90.0, 90.0, and 90.0
Space group	$P2_13$
Resolution (Å)	92.76–1.60 (1.68–1.60)
$\lambda$ (Å)	0.977
Multiplicity	38.4 (39.3)
$R_{pim}$ (all I+ & I-) (%)	4.4 (35.4)
CC (1/2)	0.999 (0.813)
Completeness (%)	100.0 (100.0)
Reflections	3,811,265 (565765)
Unique reflections	99,279 (14382)
$\langle I/\sigma(I) \rangle$	13.3 (2.4)
Reflections used in refinement	99,233
$R$ (%)	15.44
$R^{free}$ (%)	17.97
Number of atoms: protein	4112
Number of atoms: water	712
Number of atoms: ligand	18
B (Å <sup>2</sup> )	14.48
Coordinate error (ML-based) (Å)	0.15
Phase error (°)	17.08
Ramachandran favored (%)	96.39
Ramachandran allowed (%)	3.23
All-atom clash score	3.81
Bond lengths (RMSD) (Å)	0.017
Bond angles (RMSD) (°)	1.501
PDB entry	8SPK

other hand, the differences were more notable, with a conserved tryptophan in PETases being replaced by a tyrosine (Y214) in Mors1 and an aspartic acid (D153) in a position where typically glutamine or tyrosine are observed (Figure 1c). Consequently, not only is the binding subsite I changed but also the loop that connects  $\beta$ -strands 6 and 7, which migrates toward helix  $\alpha_2$ , possibly due to the electrostatic interaction between D153 and K217 (Figure 2).

The two molecules in the asymmetric unit are related by a non-crystallographic twofold. The sidechain of Y121 of chain A (Y121\_A) lies on this diad axis forcing perfect symmetry to be broken resulting in a new sidechain and main chain conformation around Y121 of chain B (Y121\_B). While Y121\_A adopts the canonical conformation observed in other PETase-like enzymes, where it



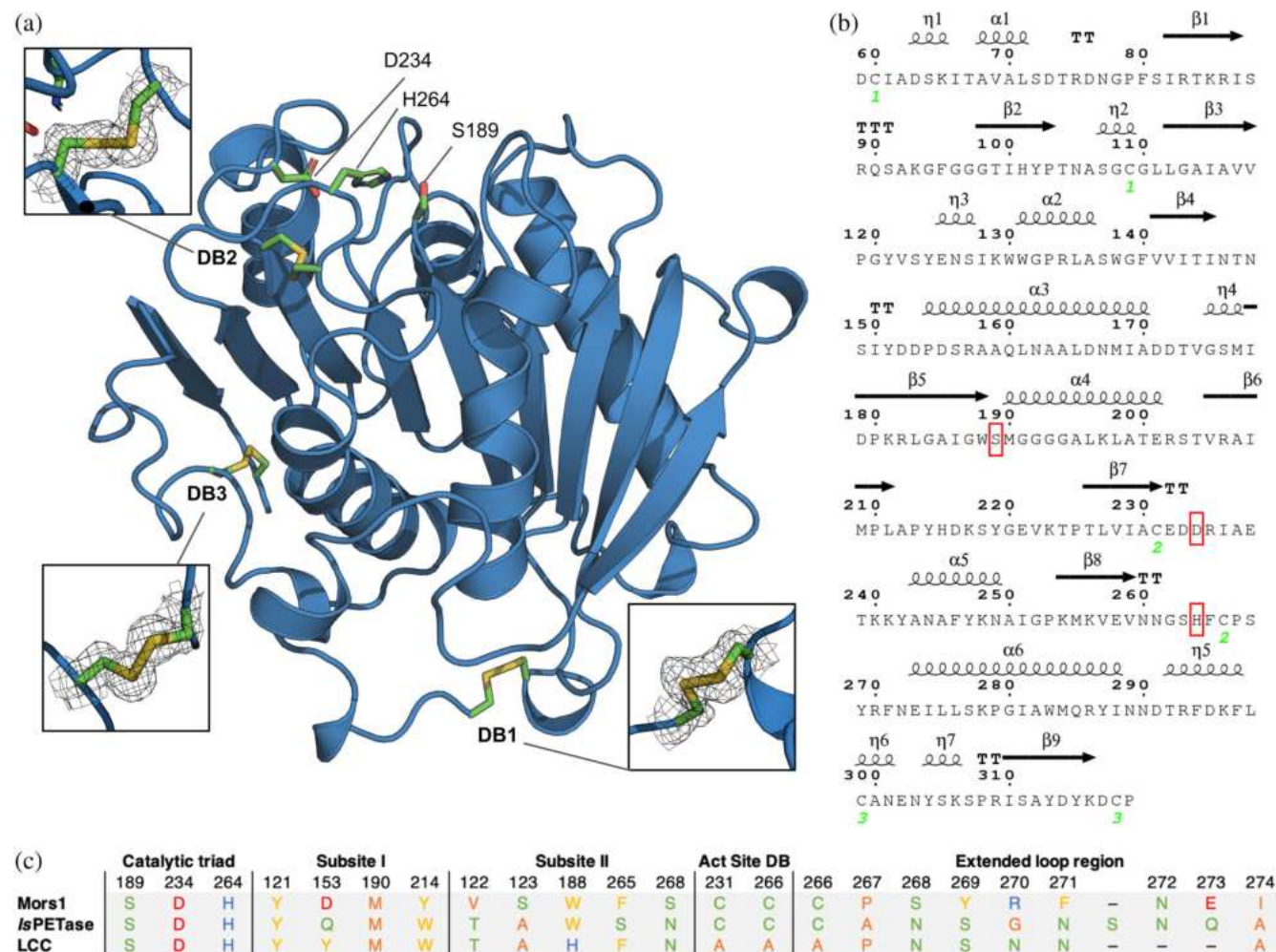


**FIGURE 1** Crystal structure and sequence of Mors1. (a) Cartoon representation of the three-dimensional structure of chain B of Mors1, with the catalytic residues and three disulfide bonds (DB) in green sticks. The insets correspond to a close-up of the three DBs, with the black mesh corresponding to the electronic density of each DB. (b) Sequence and secondary structure topology of Mors1. The red boxes indicate the location of the catalytic residues S189, D234, and H264, and the green numbers indicate the cysteines that participate in the three DBs. (c) Partial Multiple sequence alignment derived from the structural superposition of the active sites of Mors1, IsPETase (PDB 6ANE), and LCC (PDB 4EB0).

forms part of the wall of the substrate-binding pocket, Y121\_B is shifted by  $\sim 6$  Å in order to avoid the steric clash (Figure 2b). This leads to partial occlusion of the substrate binding site and requires changes to the main chain prior to the tyrosine itself, including an unusual Pro-Gly *cis* peptide bond. The absolute requirement of peptide bond isomerization for crystallization to occur potentially explains the exceptionally long time for the first crystals to appear (8 months). In this part of the map, the difference in density clearly shows signs of disorder and the overall picture that emerges is that this region of the structure may be more readily deformable than has heretofore been appreciated.

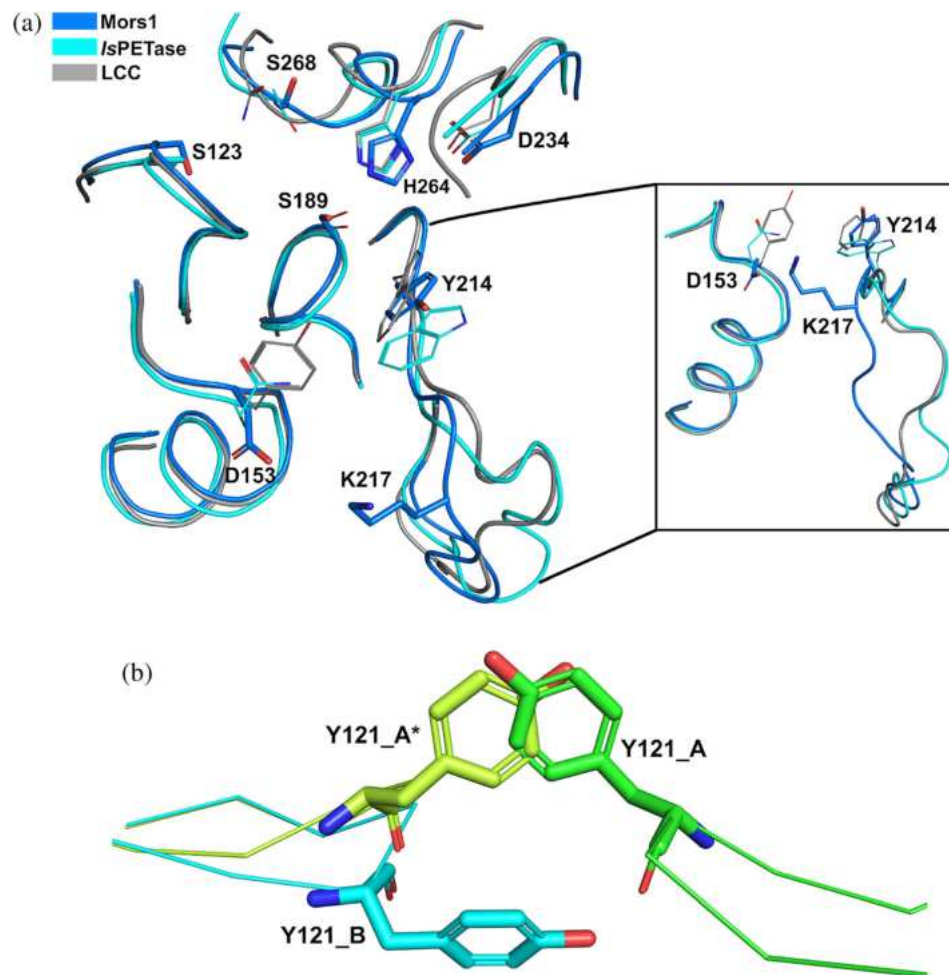
The crystal structure of Mors1 also enabled us to confirm the presence of a third disulfide bond that is unique to this enzyme and not present in IsPETase, Ple628, Ple629, or PE-H (Figure 1). As seen from the electron

density, Mors1 contains the canonical C-terminal disulfide bond between C299 and C318 present in all PETases (DB3), an active site disulfide bond between C231 and C266 that is exclusive of PETases active at moderate temperatures (DB2) and an N-terminal disulfide bond between residues C60 and C109 (DB1) that is only found in Mors1. This disulfide bond was suggested to be present in our previous work via fluorescence labeling of free cysteine thiol groups (Blázquez-Sánchez et al., 2022).

## 2.2 | Loop exchange increases optimal temperature for activity and PET degradation efficiency

Type II PET hydrolases, such as IsPETase, are characterized by having an extended loop in the active site, which is

**FIGURE 2** (a) Ribbon representation of a three-dimensional alignment of Mors1 (navy blue) with homologs LCC (gray) and *IsPETase* (cyan). The catalytic triad (S189-H264-D234) and the non-conserved residues within binding subsites 1 and 2 are shown. The inset shows a displaced loop (between  $\beta$ -strands  $\beta_6$  and  $\beta_7$ ), potentially caused by an electrostatic interaction between D153 and K217. (b) Stick representation of the different conformations observed for Y121 in chains A and B (Y121\_A1 in green and Y121\_B in cyan, respectively). In yellow, the position that Y121 would adopt in the B subunit if perfect twofold symmetry were retained (Y121\_A\*) is shown. This position was generated by applying a 180° rotation to Y121\_A, giving rise to a severe steric clash.



longer by three residues than the one in type I enzymes, such as LCC and other thermophilic homologs (Joo et al., 2018). This loop extension is also present in Mors1 (Figure 3) being one of the regions that, in MD simulations, exhibits a higher mobility within the active site in comparison to *IsPETase* (Blázquez-Sánchez et al., 2022).

For both Mors1 (Figure 3a) and *IsPETase* (Figure 3b), this loop also harbors the active site disulfide bridge that is unique to PET-degrading enzymes active near room temperature, which is required to maintain the integrity of the active site and compensate for the increased flexibility caused by the extended loop (Fecker et al., 2018). Specifically, the 15-residue region that comprises the highly flexible active site loop within Mors1 (residues 260–274, Figure 3a), which includes the  $\beta_8$ - $\alpha_6$  loop and the extended loop (residues 266–274), was replaced by the homologous 13-residue region in LCC (residues 238–250, Figure 3c). This chimeric variant, termed CM (chimeric Mors1, Figure 3d), lost the active site disulfide bridge (C231-C266) present in type II enzymes such as *IsPETase*, because the homologous loop in LCC lacks cysteine residues.

The polyesterase activity of Mors1 and CM was ascertained using polycaprolactone (PCL) nanoparticle

degradation assays (Figure 4a), which employ the aliphatic polyester PCL as a model substrate for a rapid preliminary screening in which the decrease in turbidity of a nanoparticle solution over time (Blázquez-Sánchez et al., 2022; Wei, Oeser, Then, et al., 2014). PCL degradation occurs within seconds, allowing real-time measurement using a microplate reader.

The lack of the disulfide bridge in CM leads to a total loss of enzymatic activity, as demonstrated in PCL nanoparticle degradation assays, in which no change in turbidity was observed (Figure 4a). Moreover, its elution volume in SEC experiments is significantly shifted (Figure S3). However, when the active site disulfide bridge is restored by adding the A266C substitution to CM, the respective variant (CM<sup>A266C</sup>) recovered its hydrolytic activity against PCL (Figure 4a). It is worth noting that CM<sup>A266C</sup> does not exhibit a change in oligomeric state, as ascertained by SEC (Figure S3).

We then performed PET film degradation assays, in which a PET film is incubated with an enzyme solution for hours or days, and the activity is quantified by weighing the films or by quantifying the degradation products using HPLC (Blázquez-Sánchez et al., 2022;



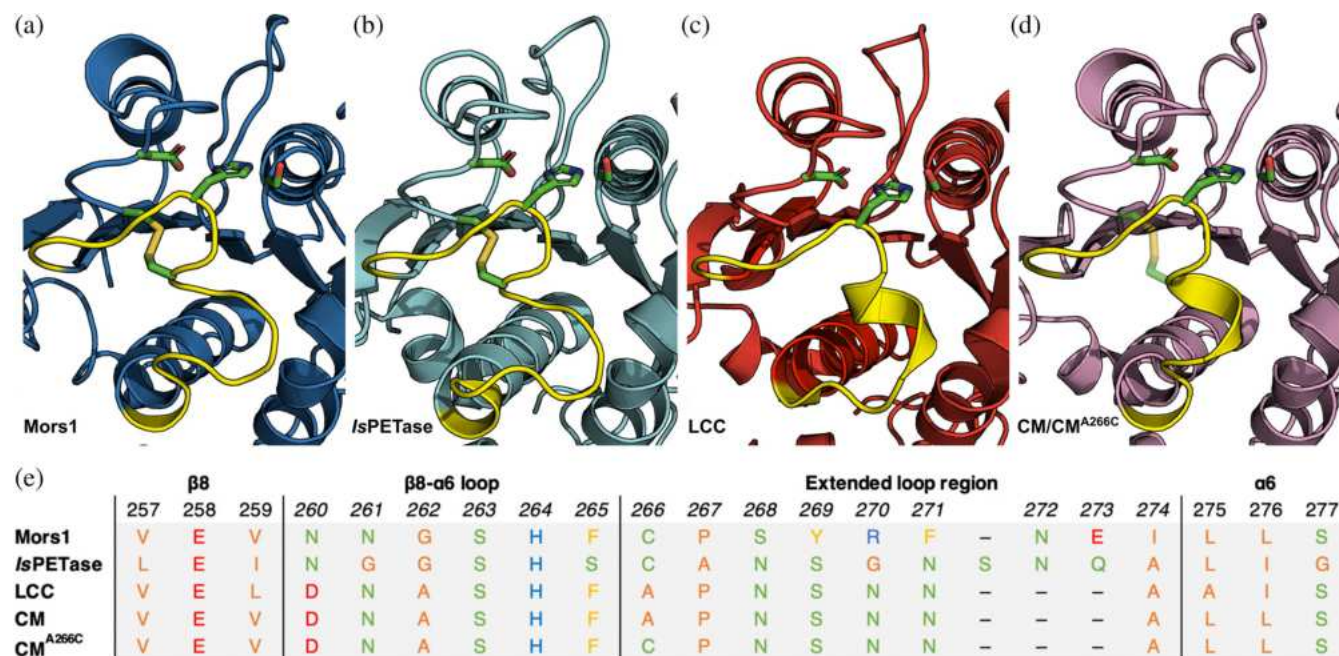


**FIGURE 3** Structure, sequence identity, and length of the extended loop in Mors1 and in other PETases. Cartoon representations depict the experimental structures of Mors1 (a, this work), *IsPETase* (b, PDB 6ANE), and LCC (c, PDB 4 EB0), and the predicted structure of the chimeric variants of Mors1 (CM and CM<sup>A266C</sup>, d) in which the  $\beta 8$ - $\alpha 6$  loop and extended loop were substituted by the equivalent regions from LCC. The disulfide bridge potentially formed in CM<sup>A266C</sup> is shown in semi-transparent sticks. In all cases, the protein is shown in cartoon representation with the  $\beta 8$ - $\alpha 6$  loop and extended loop in yellow, and the catalytic residues and the active site disulfide bond in green sticks. A multiple sequence alignment is shown in (e), showcasing the variations in sequence between these regions for Mors1, *IsPETase*, and LCC, and the chimeric Mors1 variants CM and CM<sup>A266C</sup>. Amino acids are colored by their chemistry: CNQST, green; AGILPMV, orange; RHK, blue; DE, red; FWY, yellow. Numbering corresponds to Mors1.

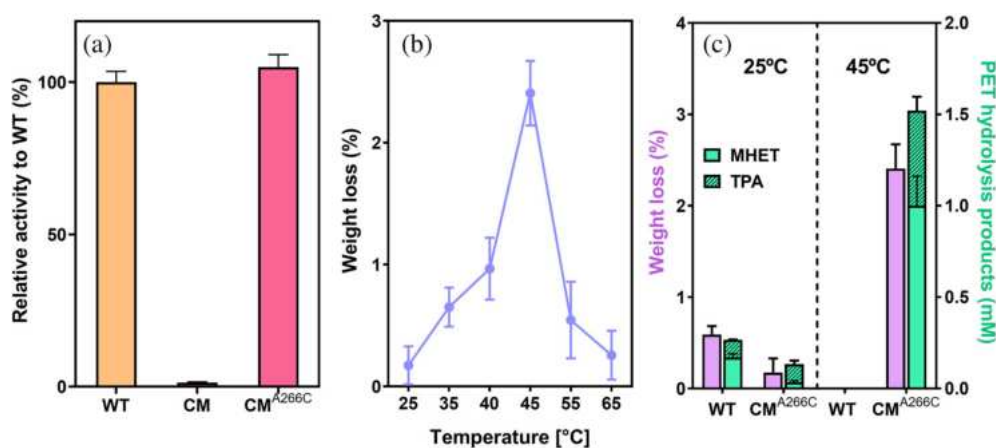


**FIGURE 4** Characterization of the polyesterase activity of loop exchanged variants of Mors1. (a) Enzymatic activity of CM and CM<sup>A266C</sup> against a PCL nanoparticle suspension, measured as a decrease in turbidity (AUs/min) at 25°C. (b) Optimal temperature for PET degradation of CM<sup>A266C</sup> measured as weight loss of PET films after a reaction time of 24 h. (c) Weight loss of PET films (pink) and HPLC quantification of TPA (dark green) and MHET (light green) released by Mors1 and CM<sup>A266C</sup> after a reaction time of 24 h at 25°C and 45°C. WT Mors1 was inactive against PET at 45°C. Mean values  $\pm$  standard deviation for  $n = 3$  experiments are shown.

Sonnendecker et al., 2022). While the activity against PCL at 25°C of CM<sup>A266C</sup> was equal to that of Mors1 (Figure 4a), it decreased against PET at the same temperature (Figure 4c). Reasoning that this could be due to a

shift in the optimal temperature for the activity of the enzyme, we determined the activity of CM<sup>A266C</sup> against PET films after incubation for 24 h at different temperatures ranging from 25°C to 65°C. These experiments

demonstrated that the optimal temperature for PET hydrolase activity of this Mors1 variant was 45°C (Figure 4b), which is 20°C higher than for Mors1 (Blázquez-Sánchez et al., 2022). It is worth noting that at this temperature, Mors1 is inactive (Figure 4c).

We then compared the activity of Mors1 and CM<sup>A266C</sup> at the optimal temperatures for both enzymes by measuring the degradation of PET films, after 24 h of incubation with 700 nM of each enzyme, both gravimetrically and by quantifying the degradation products terephthalic acid (TPA) and mono-2-hydroxyethylene terephthalate (MHET) by HPLC. Both analyses consistently inform that the activity of CM<sup>A266C</sup> is twofold lower than the activity of Mors1 at 25°C, whereas at 45°C CM<sup>A266C</sup> is 5-fold and 10-fold more active than Mors1 and CM<sup>A266C</sup> at 25°C, respectively (Figure 4c).

### 2.3 | Loop exchange only leads to local changes in structural flexibility in Mors1

Interestingly, despite this significant increase in optimal temperature for activity and PET degradation, the  $T_m$  of the CM variant or Mors1 does not change relative to the WT enzyme (Table 2), in contrast to previous studies on *IsPETase* showing that the removal of the active site disulfide bridge causes a drop of 13°C in its  $T_m$  (Joo et al., 2018). Likewise, the  $T_m$  of CM<sup>A266C</sup> is similar to that of Mors1 and the CM variant (Table 2). However, both variants do exhibit a lowering of the temperature that marks the onset of their denaturation by 6°C and 10°C for CM and CM<sup>A266C</sup>, respectively. In this regard, it is worth noting that the first derivative of the ratio of the fluorescence for CM<sup>A266C</sup> appears to present two distinct peaks, whereas the curve for CM presents a sharper peak (Figure S2). This could indicate two different populations for CM<sup>A266C</sup>, one of which is not properly folded and less thermostable, presenting this onset temperature at 36.8°C.

These results suggest that this loop exchange predominantly has a local, and not a global effect, on the protein stability, such as an increase in flexibility that has been recently reported to constitute a general feature by which the activity of several PET hydrolases can be enhanced (Chen et al., 2021; Crnjar et al., 2023). Thus, we performed 3 × 500 ns molecular dynamics (MD) simulations of Mors1 at 25 and 45°C and of CM<sup>A266C</sup> at 45°C to compare their local flexibility by ascertaining their per-residue root

mean square fluctuations (RMSF). The structure of CM<sup>A266C</sup> was predicted using ColabFold (Mirdita et al., 2022), a cloud-based version of AlphaFold2 (Jumper et al., 2021), using the experimental structure of Mors1 as a template.

On the one hand, the comparison of the simulations of Mors1 and CM<sup>A266C</sup> at their optimal temperatures for activity would enable us to detect which regions of the protein change their local flexibility due to loop swapping. On the other hand, the comparison of the simulations of Mors1 at 25°C and 45°C would enable us to disregard that these changes are influenced by the increase in temperature.

Our results from these MD simulations (Figure 5) confirm that loop exchange impacts the flexibility not only of the extended loop and covalently adjacent regions (residues 264–278), increasing their average RMSF from  $0.44 \pm 0.01$  Å to  $0.73 \pm 0.08$  Å (Figure 5a) but also of the neighboring  $\alpha$ 1- $\beta$ 1 loop (residues 64–83) and helices  $\eta$ 3 and  $\alpha$ 2 (residues 123–138), increasing their average RMSF from  $0.53 \pm 0.01$  Å to  $0.89 \pm 0.09$  Å for the former, and from  $0.41 \pm 0.01$  to  $0.61 \pm 0.08$  Å for the latter (Figure 4b). These changes are not observed when comparing Mors1 at 25°C and 45°C.

## 3 | DISCUSSION

The engineering of PET-degrading enzymes to harness their potential as biocatalysts for plastic recycling has been the subject of numerous efforts worldwide (Austin et al., 2018; Bell et al., 2022; Cui et al., 2021; Lu et al., 2022; Son et al., 2019; Tournier et al., 2020). Regardless of the use of rational design or directed evolution, most of these efforts require the screening of a vast number of variants, sometimes ranging from hundreds (Cui et al., 2021) to thousands (Bell et al., 2022).

This study serves as a proof of concept for the effectiveness of catalytic site loop exchange in enhancing the PET-degrading activity of a cold-adapted PET-degrading enzyme. In contrast, most substitutions introduced through directed evolution and machine learning in recent protein engineering studies on *IsPETase* have focused on regions outside the active site (Bell et al., 2022; Lu et al., 2022). By demonstrating the feasibility of this protein engineering strategy, we highlight its

**TABLE 2** Melting temperatures of Mors1 and its loop exchange variants determined by nano-DSF.

	Mors1	CM	CM <sup>A266C</sup>
Onset T for denaturation (°C)	46.8 ± 1.4	40.5 ± 1.6	36.8 ± 2.3
$T_m$ (°C)	57.3 ± 0.3	54.7 ± 0.2	55.7 ± 0.3

Note: Standard deviation obtained from experiments in triplicates.

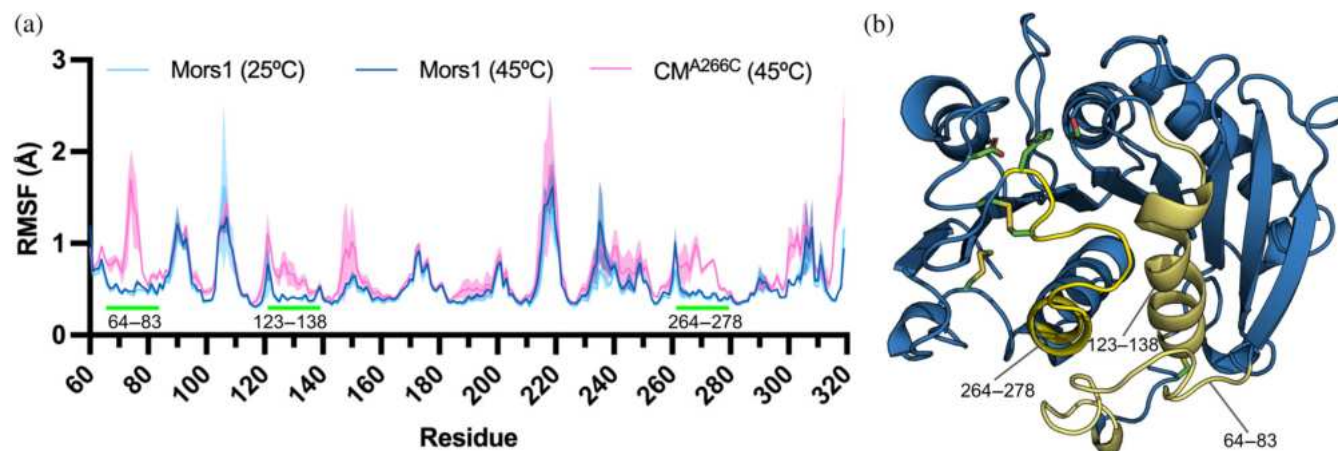


**FIGURE 5** Local structural flexibility of Mors1 and CM<sup>A266C</sup> ascertained by MD simulations. (a) RMSF from  $3 \times 500$  ns MD simulations of Mors1 at 25°C (cyan) and 45°C (blue) and CM<sup>A266C</sup> at 45°C (pink), totaling 1.5  $\mu$ s of simulation per enzyme. The lines represent the average values and the shaded contour around them corresponds to the standard deviation across the triplicates. (b) Cartoon representation of Mors1, with the regions that exhibit increases in RMSF in CM<sup>A266C</sup> shown in yellow.

potential for improving both natural and engineered enzymes.

The fivefold improvement in activity observed for CM<sup>A266C</sup> over WT Mors1 aligns well with the enhancements observed in similar research endeavors using loop exchange for the generation of chimeras with enhanced enzymatic activity, thermostability, and altered specificity. For example, Geiser et al. constructed a series of chimeras by substituting the third cytoplasmic loop of the scaffold protein bacteriorhodopsin (bR) with different lengths of the cytoplasmic loop 3 from bovine rhodopsin (Rh), with one particular chimera exhibiting a 3.5-fold increase in activity compared with the original enzyme (Geiser et al., 2006). In another work, Piper et al. developed a remarkable collection of over a dozen loop chimeras of sortases, along with several single- or double-mutant variants, focusing on the  $\beta$ 7– $\beta$ 8 loop. By profiling substrate preferences and activities, they created chimeric sortases that surpassed their WT counterparts, exhibiting up to a fourfold increase in performance and differences in substrate specificity (Piper et al., 2021).

Contrary to our expectations, the chimeric variant of Mors1, designed using a loop region from a thermophilic enzyme and exhibiting increased PET-degrading activity, also shows increased flexibility in the mutated region and in neighboring loops. This behavior can be explained, on the one hand, by the shortening of the extended loop region in CM<sup>A266C</sup>, which potentially creates a wider active site. In this regard, it has been demonstrated that the efficiency of polyester hydrolysis increases with increasing accessibility of the enzyme active site (Zumstein et al., 2017). On the other hand, the increased

flexibility can be explained by the loss of interactions between the extended loop and the neighboring regions in the chimeric variant. Recent works on thermophilic cellulases have shown that amino acid substitutions on active site loop regions based on mesophilic and psychrophilic counterparts led to enhanced flexibility and enzyme activity at moderate temperatures at the expense of hydrogen bond networks with neighboring regions (Saavedra et al., 2018). Likewise, Li et al. reported a double substitution on the active site loop of a thermophilic alcohol dehydrogenase that led to high activity at low temperature, with only slight changes in thermostability, due to increased loop flexibility and a change in backbone conformation that increased the volume of the active site (Li et al., 2017).

It is worth noting that this study primarily aims to use loop swapping to generate novel PET-degrading enzymes rather than aiming to surpass the performance of established enzymes in PET hydrolysis. Although the activity of CM<sup>A266C</sup> shows promising improvements compared with Mors1, it still falls significantly below that of thermophilic enzymes LCC and PHL7, which operate near the glass transition temperature (T<sub>g</sub>) of PET. For instance, under similar experimental conditions (500 nM enzyme, 0.55 mg<sub>enzyme</sub>·g<sub>PET</sub><sup>-1</sup>), PHL7 and LCC achieve 100% and 73% of PET film degradation at 70°C, respectively (Sonnendecker et al., 2022). However, recent research has challenged the traditional understanding that the extent of the mobility of the polyester chains below the T<sub>g</sub> is the primary factor influencing the hydrolysis rate. Remarkably, a modification of only five residues in IsPETase using rational engineering and deep learning strategies has resulted in a variant that is 1.4



times more active at 50°C than LCC at 72°C (Lu et al., 2022).

Considering these findings, the focus now shifts to determining the lowest temperature at which optimal enzymatic PET hydrolysis can be achieved. We propose that, through a combination of loop swapping and deep learning strategies, both mesophilic and psychrophilic enzymes could serve as scaffolds for mutations to enhance activity, even surpassing those observed in thermophilic enzymes, at temperatures below T<sub>g</sub>. Further work needs to be done to demonstrate which active site loops produce the largest increases in activity and whether a core set of loops can be identified as “building blocks” to enhance PET hydrolysis across diverse enzymes in a general fashion, potentially establishing a modular approach to enzyme engineering for enhanced PET degradation.

## 4 | MATERIALS AND METHODS

### 4.1 | Cloning and mutagenesis

Codon-optimized synthetic genes (Table S1) encoding His-tagged WT Mors1 (UniProt accession code P19833, residues 59–319) and a chimeric variant (CM), in which a flexible loop of the active site of Mors1 (residues 260–274) was replaced by the shorter loop of LCC (residues 238–250), were obtained from Genscript (Piscataway, NJ, USA) on a modified pET28a-TEV vector for protein expression in *E. coli* as in previous works (Blázquez-Sánchez et al., 2022).

The CM variant A266C (CM<sup>A266C</sup>) was generated by site-directed mutagenesis, using the primers listed in Table S2. The PCR reaction mixture (20 µL) contained 0.02 U/µl Phusion DNA polymerase (Thermo Scientific, Waltham, MA, USA), 0.2 mM dNTP mix, 1 µL of template plasmid (50–100 ng/µl), 10 µM primers, 1× Phusion buffer, and ultrapure water. The PCR cycles were as follows: initial denaturation at 98°C for 30 s; 22 cycles of 98°C for 5 s, 63°C for 15 s, and 72°C for 5 min; and a final elongation at 72°C for 2 min. The reaction products were then treated with DpnI restriction enzyme (New England Biolabs GmbH, Germany) at 37°C for 90 min to degrade the template plasmid and transformed into XL10-Gold ultracompetent *E. coli* cells (Agilent Technologies, Santa Clara, CA, USA). Cells were plated out into LB agar plates containing 37 µg/mL kanamycin and incubated overnight at 37°C. Then, positive colonies were cultured overnight at 37°C in LB media supplemented with kanamycin for plasmid extraction using the Monarch Plasmid Miniprep Kit (New England Biolabs GmbH, Germany) and DNA sequencing.

### 4.2 | Protein expression and purification

Recombinant expression and purification of WT Mors1, CM, and CM<sup>A266C</sup> for characterization of its PCL- and PET-degrading activity was performed as in previous works (Blázquez-Sánchez et al., 2022). Briefly, *E. coli* BL21 (DE3) cells transformed with each plasmid were cultured in Terrific Broth media (Thermo Fisher Scientific, Waltham, MA, USA) containing 37 µg/mL kanamycin at 37°C with vigorous shaking. Upon reaching an optical density at 600 nm (OD<sub>600</sub>) of 0.8, 1 mM isopropyl β-D-1-thiogalactopyranoside (IPTG) was added, and the bacterial culture was further grown for 16 h at 14°C. Then, cells were harvested by centrifugation (3200 × g, 4°C, 30 min), resuspended, and sonicated in lysis buffer (50 mM sodium phosphate pH 8.0, 20 mM imidazole, 200 mM NaCl, 8 M urea) and centrifuged (24,000 × g, 4°C, 60 min). The resulting cleared lysate was loaded onto a Ni-Sepharose resin (HisTrap FF crude, Cytiva Life Sciences, Marlborough, MA, USA) for immobilized metal affinity chromatography, and the denatured His-tagged protein was eluted using the lysis buffer supplemented with 350 mM imidazole. Finally, the purified enzyme was refolded by dialysis against 50 mM sodium phosphate pH 8.0, 200 mM NaCl, and 200 mM arginine. Purity analysis of the enzyme solution was ascertained by SDS-PAGE in 15% polyacrylamide gels (Tris-glycine buffer) using a prestained molecular marker (PS10 PLUS; 11–180 kDa, Gene On, Ludwigshafen, Germany).

For protein crystallization, the purification protocol was further optimized to obtain soluble expression of Mors1. *E. coli* Origami2 (DE3) cells harboring pET28a-TEV-Mors1 were grown at 37°C in TB medium supplemented with 50 µg/mL kanamycin, 13 µg/mL tetracycline and 50 µg/mL streptomycin. Once an OD<sub>600</sub> = 0.6–0.8 was reached, the culture was cooled to 15°C, and the protein expression was induced by adding 0.3 mM IPTG. After 16 h, cells were harvested by centrifugation at 10,000 × g for 45 min at 4°C and suspended in lysis buffer (50 mM Tris-HCl pH 7.5, 300 mM NaCl, 0.05% β-mercaptoethanol, 5% v/w glycerol, 0.1 mM PMSF). The soluble fraction, after cell lysis by sonication, was isolated by centrifugation at 16,000 × g for 45 min at 4°C. Then, the soluble fraction was loaded onto a column with 5 mL His60 Ni-Superflow Resin (Clontech Laboratories, Palo Alto, CA, USA) previously equilibrated with lysis buffer. Subsequently, the resin was washed with 5 column volumes (CV) of lysis buffer and 5 CV of lysis buffer supplemented with 50 mM imidazole. The proteins were eluted using 2 CV of lysis buffer (without glycerol) containing 250 mM imidazole. The protein-containing fractions were subjected to SEC using a Superdex 200 XK-16 column (GE Healthcare) pre-equilibrated

in SEC buffer (150 mM NaCl, 20 mM Tris-HCl pH 7.5). The protein was monitored at 280 nm and all fractions were collected for purity analysis by SDS-PAGE. The desired concentration for each experiment was then achieved by performing cycles of concentration at  $800 \times g$  and  $18^\circ\text{C}$ , using an Amicon Ultra centrifugal filter (Merck KGaA, Darmstadt, Germany) with a 30-kDa cutoff.

#### 4.2.1 | SEC-MALS

The oligomeric state of Mors1 was evaluated using a miniDAWN TREOS three-angle light scattering detector and Optilab T-rEX refractometer (Wyatt Technology, Santa Barbara, CA, USA). This system was coupled to a Waters 600 HPLC system (Waters) for the SEC step. A total of 50  $\mu\text{L}$  of sample at 1 mg/ml – 1 was loaded onto a Superdex 75 10/300 GL column (GE Healthcare) equilibrated in 20 mM Tris (pH 7.8), 300 mM NaCl. The data collection and analysis were performed using the ASTRA7 software (Wyatt Technology).

### 4.3 | X-ray crystallography, structure determination, and refinement

Mors1 crystallization assays were carried out by using the automated sitting-drop vapor diffusion technique, employing the Crystal Gryphon robot (Art Robbins Instruments, Sunnyvale, CA, USA). The plates used were Intelli-plate 96-low profile (Art Robbins Instruments) and Swissci 96-Well (Molecular Dimensions Inc., Holland, OH, USA). To promote the formation of crystals, commercial kits MORPHEUS (Molecular Dimensions), JCSG+Suite (Qiagen Sciences, Germantown, MD, USA), BCS (Molecular Dimensions), SG1 TM Screen (Molecular Dimensions) and Index (Hampton Research, Aliso Viejo, CA, USA) were used. Each of the 96 kit conditions was tested at three different protein concentrations (1.2 mg/mL, 1.0 mg/mL, and 0.8 mg/mL) using a 1:1 ratio of protein and precipitant solution. The final volume of each drop was 0.6  $\mu\text{L}$ , with 50  $\mu\text{L}$  of solution in the reservoir. The plates were sealed with an adhesive film, stored in the Rock Imager 1000 plate hotel (Formulatrix, Bedford, MA, USA), and incubated at  $20^\circ\text{C}$ . Crystals appeared after 8 months of incubation in SG1<sup>TM</sup>-C2 condition (1.4 M sodium malonate dibasic monohydrate at pH 7.0) with 0.8 mg/mL of protein and were harvested and cryo-cooled in liquid nitrogen for data collection. The x-ray diffraction data were collected at 100 K on the Sirius synchrotron (LNLS-CNPEM, Campinas) using beamline Manacá housing a PILATUS 2 M detector.

Indexation, integration, and data reduction/scaling were done by autoPROC (Vonrhein et al., 2018). Molecular replacement was carried out by Phaser (McCoy et al., 2007), using an AlphaFold2-predicted model of Mors1 as a search model (Jumper et al., 2021; Mirdita et al., 2022). Alternate rounds of refinement and model building were conducted using *phenix.refine* (Adams et al., 2010) and Coot (Emsley & Cowtan, 2004). Data collection, refinement statistics, and PDB code are summarized in Table 1.

### 4.4 | Thermal stability

The  $T_m$  of WT Mors1, CM, and CM<sup>A266C</sup> were determined by nano-differential scanning fluorimetry (nanoDSF). In these experiments, a thin glass capillary was filled with purified enzyme at a concentration of  $\sim 150 \mu\text{g/mL}$  in 20 mM HEPES pH 7.5, 70 mM NaCl, and heated from  $20^\circ\text{C}$  to  $95^\circ\text{C}$  at a rate of  $1^\circ\text{C}/\text{min}$  (nanoDSF, Prometheus NT.48, Nanotemper Technologies, Munich, Germany). The intrinsic fluorescence emission of tryptophan residues was monitored at 330 and 350 nm, and the first derivative of the ratio of fluorescence at 330 and 350 nm was calculated to obtain the apparent  $T_m$ .

### 4.5 | PCL nanoparticle degradation assays

PCL nanoparticles were prepared by dissolving 250 mg of poly- $\epsilon$ -caprolactone (PCL) (Sigma-Aldrich, San Luis, MO, USA) in 10 mL acetone at  $50^\circ\text{C}$ , followed by dropwise pouring the solution into 100 mL of distilled water under strong stirring and then filtering with a paper filter. Residual acetone was evaporated by overnight incubation at  $50^\circ\text{C}$ . The PCL nanoparticles were used to measure the polyesterase activity of WT Mors1 and its chimeric variants at  $25^\circ\text{C}$  on a Synergy Mx microplate reader (Biotek Instruments, Vermont, USA) by turbidimetric analysis, as described in previous works (Wei, Oeser, Barth, et al., 2014; Wei, Oeser, Then, et al., 2014). In these experiments, each well in the microplate contains 66  $\mu\text{L}$  of a solution of 20  $\mu\text{g/mL}$  of each enzyme in 125 mM sodium phosphate pH 8.0, 200 mM NaCl. Reactions are started by adding 134  $\mu\text{L}$  of a 0.07 mg/mL PCL nanoparticle suspension, completing a total volume of 200  $\mu\text{L}$  such that the initial  $\text{OD}_{600}$  is 0.8. The enzymatic hydrolysis of the PCL nanoparticles was monitored by following the decrease in turbidity of the solution by  $\text{OD}_{600}$ . The initial rates of hydrolysis are determined as the slope of the linear region of the graphs of decreasing  $\text{OD}_{600}$  as a function of time.

## 4.6 | Hydrolysis of amorphous PET films

Amorphous PET films (0.5 cm × 3 cm, 250 μm thickness; ~ 45 mg, product number ES301445, Goodfellow, Hamburg, Germany) were washed, weighted, and placed in 2 mL reaction tubes in a solution containing 1 M potassium phosphate pH 8.0, 200 mM NaCl and 700 nM of WT Mors1 or CM<sup>A266C</sup> (0.8 μg<sub>enzyme</sub>·g<sub>PET</sub><sup>-1</sup>). Hydrolysis reactions were performed for 24 h at different temperatures. PET films were washed with water, aqueous 0.5% SDS and ethanol and dried at 50°C overnight. Weight loss was measured gravimetrically. The products of degradation, terephthalic acid (TPA) and mono(2-hydroxyethyl) terephthalate (MHET), were quantified by HPLC (Agilent 1100 Series HPLC instrument; Agilent Technologies, La Jolla, CA, USA), using a C18 column (Europer II 100–5; 150 × 2 mm with pre-column, Knauer Wissenschaftliche Geräte GmbH, Berlin, Germany), following a previously described protocol (Blázquez-Sánchez et al., 2022). Briefly, samples were run at a flow rate of 0.3 mL/min using a gradient of acetonitrile with 0.1% formic acid (A) and aqueous solution with 0.1% formic acid (B) as follows: 95% B (0.0 min), 80% B (0.1 min), 76% B (3.0 min), 60% B (3.1 min), 0% B (8.0 min), hold for 2 min and back to 95% B (analysis time 12.0 min). The injection volume of the sample was 2 μL and the products were detected by their absorbance at 241 nm, using the retention times of TPA (Sigma Aldrich, St. Louis, MO, USA) and MHET as standards. MHET was synthesized via hydrolysis of bis(hydroxyethyl) terephthalate (BHET) (Sigma Aldrich, St. Louis, MO, USA) with KOH (Palm et al., 2019).

## 4.7 | MD simulations

Molecular dynamics simulations of Mors1 and CM<sup>A266C</sup> were performed using the AMBER20 simulation package (Case et al., 2020) along with the ff19SB force field (Tian et al., 2020). For the WT enzyme, the crystal structure solved in this work was used as initial coordinates. For CM<sup>A266C</sup>, an initial structure was obtained using ColabFold (Mirdita et al., 2022), a cloud-based version of AlphaFold2 (Jumper et al., 2021), using default parameters and using the experimental structure of Mors1 as a template.

For the system preparation, the protonation state of each residue in each protein at pH 8.0 was first estimated using the H++ server and PlayMolecule (Gordon et al., 2005; Martínez-Rosell et al., 2017). Then, each system was placed in a truncated octahedral box with 1.5 nm of padding, solvated using OPC water molecules, and neutralized using counter ions. The final system was

treated with periodic boundary conditions and minimized first using a steepest descent method with position restraints on water and ions, followed by a second step without any restraints. For the equilibration step, each system was heated from 0 to 298 K or 318 K, depending on the target temperature, for 150 ps at constant volume using a Langevin thermostat, followed by equilibration for 1 ns at constant temperature and pressure of 1 bar using a Berendsen barostat while restraining the protein atoms, and lastly 1 ns without any restraints. MD production runs were carried out in three replicas of 500 ns for each system, totaling 1.5 μs of simulation for each enzyme, using a time step of 2.0 fs alongside the SHAKE algorithm (Ryckaert et al., 1977) and a 10 Å nonbonded cutoff. Independent runs were ensured using random seeds for initial velocities during the equilibration steps.

The MD simulation replicates for each system were checked for convergence using the backbone root-mean-square deviation (RMSD) using the first frame as a reference, followed by calculating the per-residue root mean square fluctuations (RMSF). Both analyses were executed using CPPTRAJ of AmberTools20 (Case et al., 2020).

## AUTHOR CONTRIBUTIONS

**Paula Blázquez-Sánchez:** Conceptualization (supporting); Data Curation (lead); Formal Analysis (lead); Funding Acquisition (supporting); Investigation (lead); Methodology (equal); Visualization (equal); Writing—Original Draft Preparation (supporting). **Jhon A. Vargas:** Methodology (supporting); Data Curation (supporting); Formal Analysis (supporting). Writing—Original Draft Preparation (supporting). **Adriano A. Furtado:** Methodology (supporting); Data Curation (supporting); Formal Analysis (supporting); Writing—Original Draft Preparation (supporting). **Aransa Griñen:** Data Curation (supporting); Formal Analysis (supporting); Investigation (supporting); Methodology (supporting); Visualization (supporting); Writing—Original Draft Preparation (supporting). **Diego A. Leonardo:** Methodology (supporting); Data Curation (supporting); Formal Analysis (supporting); Writing—Original Draft Preparation (supporting). **Susana A. Sculaccio:** Methodology (supporting); Data Curation (supporting); Formal Analysis (supporting). **Humberto D'Muniz Pereira:** Formal Analysis (supporting); Funding Acquisition (supporting); Methodology (supporting); Resources (equal); Writing—Original Draft Preparation (supporting). **Christian Sonnendecker:** Conceptualization (supporting); Methodology (supporting); Resources (supporting); Writing—Original Draft Preparation (supporting). **Wolfgang Zimmermann:** Conceptualization (supporting); Methodology (supporting); Resources (supporting); Writing—



Original Draft Preparation (supporting). **Beatriz Díez**: Conceptualization (supporting); Funding Acquisition (supporting); Writing—Original Draft Preparation (supporting). **Richard C. Garratt**: Conceptualization (supporting); Formal Analysis (supporting); Funding Acquisition (equal); Methodology (supporting); Resources (equal); Writing—Original Draft Preparation (supporting). **César A. Ramírez-Sarmiento**: Conceptualization (lead); Data Curation (supporting); Formal Analysis (supporting); Funding Acquisition (equal); Investigation (supporting); Methodology (equal); Resources (equal); Visualization (equal); Writing—Original Draft Preparation (lead).

## ACKNOWLEDGMENTS

This research was funded by the National Agency for Research and Development (ANID) and the São Paulo Research Foundation through the International Cooperation Program (PCI ANID-FAPESP 2019/13259-9), the ANID Millennium Science Initiative Program (ICN17\_022 and ICN2021\_044), and a Doctoral Thesis Support Grant from Instituto Antártico Chileno (INACH) to Paula Blázquez-Sánchez (DG\_11\_18) and an INACH Regular Grant to Beatriz Díez (RT\_04\_19). Paula Blázquez-Sánchez and Aransa Griñen were supported by ANID doctoral scholarships (PFCHA 21191979 and 21220450) and Adriano A. Furtado by a CAPES Masters' scholarship (88887.635854/2021-00). Powered@NLHPC: This research was partially supported by the supercomputing infrastructure of the NLHPC (ECM-02). This research used facilities at the Brazilian Synchrotron Light Laboratory (LNLS), part of the Brazilian Center for Research in Energy and Materials (CNPEM), a private non-profit organization under the supervision of the Brazilian Ministry for Science, Technology, and Innovation (MCTI). The Manacá beamline staff is acknowledged for assistance during the diffraction data collection experiments (project proposal 20220741).

## CONFLICT OF INTEREST STATEMENT

The authors declare no conflict of interest exists.

## ORCID

Paula Blázquez-Sánchez  <https://orcid.org/0000-0003-3232-909X>

Jhon A. Vargas  <https://orcid.org/0000-0002-4946-1807>

Adriano A. Furtado  <https://orcid.org/0009-0009-7565-3413>

Diego A. Leonardo  <https://orcid.org/0000-0003-4264-3074>

Susana A. Sculaccio  <https://orcid.org/0009-0008-1495-4813>


Humberto D'Muniz Pereira  <https://orcid.org/0000-0002-8652-6729>

8652-6729

Christian Sonnendecker  <https://orcid.org/0000-0001-7904-7343>

Wolfgang Zimmermann  <https://orcid.org/0000-0002-5730-6663>

Beatriz Díez  <https://orcid.org/0000-0002-9371-8083>

Richard C. Garratt  <https://orcid.org/0000-0002-2016-3179>

César A. Ramírez-Sarmiento  <https://orcid.org/0000-0003-4647-903X>

## REFERENCES

- Adams PD, Afonine PV, Bunkóczi G, Chen VB, Davis IW, Echols N, et al. PHENIX: a comprehensive python-based system for macromolecular structure solution. *Acta Crystallogr D Biol Crystallogr*. 2010;66:213–21.
- Austin HP, Allen MD, Donohoe BS, Rorrer NA, Kearns FL, Silveira RL, et al. Characterization and engineering of a plastic-degrading aromatic polyesterase. *Proc Natl Acad Sci U S A*. 2018;115:E4350–7.
- Bell EL, Smithson R, Kilbride S, Foster J, Hardy FJ, Ramachandran S, et al. Directed evolution of an efficient and thermostable PET depolymerase. *Nat Catal*. 2022;5:673–81.
- Blázquez-Sánchez P, Engelberger F, Cifuentes-Anticevic J, Sonnendecker C, Griñen A, Reyes J, et al. Antarctic polyester hydrolases degrade aliphatic and aromatic polyesters at moderate temperatures. *Appl Environ Microbiol*. 2022;88:e0184221.
- Bollinger A, Thies S, Knieps-Grünhagen E, Gertzen C, Kobus S, Höppner A, et al. A novel polyester hydrolase from the marine bacterium structural and functional insights. *Front Microbiol*. 2020;11:114.
- Case DA, Belfon K, Ben-Shalom IY, Brozell SR, Cerutti DS, Cheatham TE III, et al. AMBER 2020. San Francisco: University of California; 2020.
- Chen C-C, Han X, Li X, Jiang P, Niu D, Ma L, et al. General features to enhance enzymatic activity of poly(ethylene terephthalate) hydrolysis. *Nat Catal*. 2021;4:425–30.
- Crnjar A, Griñen A, Kamerlin SCL, Ramírez-Sarmiento CA. Conformational selection of a tryptophan side chain drives the generalized increase in activity of PET hydrolases through a Ser/Ile double mutation. *ACS Org Inorg Au*. 2023;3:109–19.
- Cui Y, Chen Y, Liu X, Dong S, Tian Y, Qiao Y, et al. Computational redesign of a PETase for plastic biodegradation under ambient condition by the GRAPE strategy. *ACS Catal*. 2021;11:1340–50.
- Drummond DA, Silberg JJ, Meyer MM, Wilke CO, Arnold FH. On the conservative nature of intragenic recombination. *Proc Natl Acad Sci U S A*. 2005;102:5380–5.
- Emsley P, Cowtan K. Coot: model-building tools for molecular graphics. *Acta Crystallogr D Biol Crystallogr*. 2004;60:2126–32.
- Fecker T, Galaz-Davison P, Engelberger F, Narui Y, Sotomayor M, Parra LP, et al. Active site flexibility as a Hallmark for efficient PET degradation by *I. sakaiensis* PETase. *Biophys J*. 2018;114:1302–12.
- Geiser AH, Sievert MK, Guo L-W, Grant JE, Krebs MP, Fotiadis D, et al. Bacteriorhodopsin chimeras containing the third cytoplasmic loop of bovine rhodopsin activate transducin for GTP/GDP exchange. *Protein Sci*. 2006;15:1679–90.

- Geyer R, Jambeck JR, Law KL. Production, use, and fate of all plastics ever made. *Sci Adv*. 2017;3:e1700782.
- Gordon JC, Myers JB, Folta T, Shoja V, Heath LS, Onufriev A. H<sup>+</sup>: a server for estimating pK<sub>a</sub>s and adding missing hydrogens to macromolecules. *Nucleic Acids Res*. 2005;33:W368–71.
- Joo S, Cho IJ, Seo H, Son HF, Sagong H-Y, Shin TJ, et al. Structural insight into molecular mechanism of poly(ethylene terephthalate) degradation. *Nat Commun*. 2018;9:382.
- Jumper J, Evans R, Pritzel A, Green T, Figurnov M, Ronneberger O, et al. Highly accurate protein structure prediction with AlphaFold. *Nature*. 2021;596:583–9.
- Krissinel E, Henrick K. Inference of macromolecular assemblies from crystalline state. *J Mol Biol*. 2007;372:774–97.
- Li G, Maria-Solano MA, Romero-Rivera A, Osuna S, Reetz MT. Inducing high activity of a thermophilic enzyme at ambient temperatures by directed evolution. *Chem Commun*. 2017;53:9454–7.
- Li Z, Zhao Y, Wu P, Wang H, Li Q, Gao J, et al. Structural insight and engineering of a plastic degrading hydrolase Ple629. *Biochem Biophys Res Commun*. 2022;626:100–6.
- Lu H, Diaz DJ, Czarnecki NJ, Zhu C, Kim W, Shroff R, et al. Machine learning-aided engineering of hydrolases for PET depolymerization. *Nature*. 2022;604:662–7.
- Martínez-Rosell G, Giorgino T, De Fabritiis G. PlayMolecule Protein-Prepare: a web application for protein preparation for molecular dynamics simulations. *J Chem Inf Model*. 2017;57:1511–6.
- McCoy AJ, Grosse-Kunstleve RW, Adams PD, Winn MD, Storoni LC, Read RJ. Phaser crystallographic software. *J Appl Cryst*. 2007;40:658–74.
- Meyer Cifuentes IE, Wu P, Zhao Y, Liu W, Neumann-Schaal M, Pfaff L, et al. Molecular and biochemical differences of the tandem and cold-adapted PET hydrolases Ple628 and Ple629, isolated from a marine microbial consortium. *Front Bioeng Biotechnol*. 2022;10:930140.
- Mirdita M, Schütze K, Moriwaki Y, Heo L, Ovchinnikov S, Steinegger M. ColabFold: making protein folding accessible to all. *Nat Methods*. 2022;19:679–82.
- Mueller R-J. Biological degradation of synthetic polyesters—enzymes as potential catalysts for polyester recycling. *Process Biochem*. 2006;41:2124–8.
- Nestl BM, Hauer B. Engineering of flexible loops in enzymes. *ACS Catal*. 2014;4:3201–11.
- Palm GJ, Reisky L, Böttcher D, Müller H, Michels EAP, Walczak MC, et al. Structure of the plastic-degrading *Ideonella sakaiensis* MHE-Tase bound to a substrate. *Nat Commun*. 2019;10:1717.
- Piper IM, Struyvenberg SA, Valgardson JD, Johnson DA, Gao M, Johnston K, et al. Sequence variation in the  $\beta$ 7- $\beta$ 8 loop of bacterial class a sortase enzymes alters substrate selectivity. *J Biol Chem*. 2021;297:100981.
- Romero PA, Arnold FH. Exploring protein fitness landscapes by directed evolution. *Nat Rev Mol Cell Biol*. 2009;10:866–76.
- Ryckaert J-P, Ciccotti G, Berendsen HJC. Numerical integration of the cartesian equations of motion of a system with constraints: molecular dynamics of n-alkanes. *J Comput Phys*. 1977;23:327–41.
- Saavedra JM, Azócar MA, Rodríguez V, Ramírez-Sarmiento CA, Andrews BA, Asenjo JA, et al. Relevance of local flexibility near the active site for enzymatic catalysis: biochemical characterization and engineering of cellulase Cel5A from bacillus agaradherans. *Biotechnol J*. 2018;13:e1700669.
- Schyns ZOG, Shaver MP. Mechanical recycling of packaging plastics: a review. *Macromol Rapid Commun*. 2021;42:e2000415.
- Shroff R, Cole AW, Diaz DJ, Morrow BR, Donnell I, Annapareddy A, et al. Discovery of novel gain-of-function mutations guided by structure-based deep learning. *ACS Synth Biol*. 2020;9:2927–35.
- Son HF, Cho IJ, Joo S, Seo H, Sagong H-Y, Choi SY, et al. Rational protein engineering of thermo-stable PETase from *Ideonella sakaiensis* for highly efficient PET degradation. *ACS Catal*. 2019;9:3519–26.
- Sonnendecker C, Oeser J, Richter PK, Hille P, Zhao Z, Fischer C, et al. Low carbon footprint recycling of post-consumer PET plastic with a metagenomic polyester hydrolase. *ChemSusChem*. 2022;15:e202101062.
- Tian C, Kasavajhala K, Belfon KAA, Raguette L, Huang H, Miguez AN, et al. ff19SB: amino-acid-specific protein backbone parameters trained against quantum mechanics energy surfaces in solution. *J Chem Theory Comput*. 2020;16:528–52.
- Tournier V, Topham CM, Gilles A, David B, Folgoas C, Moya-Leclair E, et al. An engineered PET depolymerase to break down and recycle plastic bottles. *Nature*. 2020;580:216–9.
- Vonrhein C, Tickle IJ, Flensburg C, Keller P, Paciorek W, Sharff A, et al. Advances in automated data analysis and processing within autoPROC, combined with improved characterisation, mitigation and visualisation of the anisotropy of diffraction limits using STARANISO. *Acta Crystallogr A Found Adv*. 2018;74:a360.
- Wei R, Oeser T, Barth M, Weigl N, Lübs A, Schulz-Siegmund M, et al. Turbidimetric analysis of the enzymatic hydrolysis of polyethylene terephthalate nanoparticles. *J Mol Catal B: Enzym*. 2014;103:72–8.
- Wei R, Oeser T, Then J, Kühn N, Barth M, Schmidt J, et al. Functional characterization and structural modeling of synthetic polyester-degrading hydrolases from *Thermomonospora curvata*. *AMB Express*. 2014;4:44.
- Wei R, Zimmermann W. Biocatalysis as a green route for recycling the recalcitrant plastic polyethylene terephthalate. *J Microbial Biotechnol*. 2017;10:1302–7.
- Yoshida S, Hiraga K, Takehana T, Taniguchi I, Yamaji H, Maeda Y, et al. A bacterium that degrades and assimilates poly(ethylene terephthalate). *Science*. 2016;351:1196–9.
- Zumstein MT, Rechsteiner D, Roduner N, Perz V, Ribitsch D, Guebitz GM, et al. Enzymatic hydrolysis of polyester thin films at the nanoscale: effects of polyester structure and enzyme active-site accessibility. *Environ Sci Technol*. 2017;51:7476–85.

## SUPPORTING INFORMATION

Additional supporting information can be found online in the Supporting Information section at the end of this article.

**How to cite this article:** Blázquez-Sánchez P, Vargas JA, Furtado AA, Griñen A, Leonardo DA, Sculaccio SA, et al. Engineering the catalytic activity of an Antarctic PET-degrading enzyme by loop exchange. *Protein Science*. 2023;32(9):e4757. <https://doi.org/10.1002/pro.4757>